J. Fluid Mech. (2005), *vol.* 530, *pp.* 265–293.
doi:10.1017/S0022112005003708 Printed in the United Kingdom

Transition mechanisms in a three-dimensional boundary-layer flow with pressure-gradient changeover

By PETER WASSERMANN AND MARKUS KLOKER

Institut für Aerodynamik und Gasdynamik, Universität Stuttgart, Pfaffenwaldring 21, D-70550 Stuttgart, Germany

(Received 2 February 2004 and in revised form 14 December 2004)

The laminar breakdown of a three-dimensional flat-plate boundary-layer flow with favourable and ensuing adverse pressure gradient (APG), generic for an infinite swept wing, is investigated in detail by means of spatial direct numerical simulations. Emphasis is on transition mechanisms in the region of adverse pressure gradient where the undistorted laminar base flow also becomes unstable with respect to Tollmien–Schlichting (TS) waves that are most amplified if two-dimensional with respect to the local streamwise direction. The influence of finite-amplitude crossflow vortices, coming from the region of favourable pressure gradient, on the TS instability properties is investigated. It turns out that crossflow-vortex-induced secondary instabilities are the most amplified disturbances even for low-amplitude vortex modes. The TS waves act as generators of fundamental low-frequency secondary modes, but are neither important for their growth nor for breakdown. As for active disturbance control, any method aiming at attenuating two-dimensional TS waves must fail. On the other hand, the passive upstream-flow-deformation technique also delays transition in the APG region.

1. Introduction

The initially laminar flow past a swept-back wing is typically susceptible to four types of primary instability. The attachment-line flow is subject to Görtler–Hämmerlin (GH) instabilities, and in the subsequent downstream region of favourable pressure gradient (FPG), crossflow (CF) instabilities dominate before, in the region of adverse pressure gradient (APG), Tollmien–Schlichting (TS) instabilities arise. At concave surface curvature the centrifugal Görtler-instability can be present, but more unlikely this is the larger the sweep angle is. In this paper, we concentrate on the flow on the suction side downstream of the leading-edge region with negligible surface curvature, i.e. we focus on CF and TS instabilities, their occurrence, amplification and interaction, especially in the region of changeover from favourable to adverse pressure gradient.

The chordwise acceleration of the flow on the wing's suction side induces an inboard-oriented crossflow component inside the boundary layer, perpendicular to the mean flow direction. The crossflow velocity profile $w_s(y)$, y being the wall-normal coordinate, is inflectional and causes a strong primary instability of the flow with respect to so-called CF modes. The wavenumber vectors of both unsteady and steady CF modes – the latter referred to as CF vortices – are oriented approximately parallel to the crossflow direction, i.e. perpendicular to the outer streamline. The issue of how

the three-dimensional stagnation flow, subject to unstable unsteady GH modes very close to the attachment line (see, e.g. Theofilis *et al.* 2003), gives rise to dominating CF instability downstream has been investigated by Bertolotti (2000).

At the point of pressure gradient changeover from FPG to APG, the curvature of the outer streamline changes sign, and with some downstream lag the direction of the crossflow changes in the near-wall region as well. Thus, the crossflow velocity profiles $w_s(y)$ are s-shaped here. Owing to the adverse pressure gradient, inflectional streamwise velocity profiles $u_s(y)$ are present that also give rise to TS instabilities. In contrast to the CF modes, the wavenumber vectors of the most amplified TS modes are nearly aligned with the outer streamline.

In experiments and in free flight, early transition in the FPG region of a swept-back wing is typically observed. Therefore most investigations concerning transition put major emphasis on this crossflow-induced transition, and the working mechanisms are well understood. The subject has been tackled by means of controlled transition experiments, elaborated theoretical methods and direct numerical simulations. For an overview see Saric, Reed & White (2003), and for more details, e.g. Koch *et al.* (2000) and Wassermann & Kloker (2002). At low freestream-turbulence conditions as in free flight, steady crossflow vortex modes excited by (minute) surface non-uniformity or roughness are found to be dominant, although the maximal primary amplification is for unsteady disturbances. Consequently, most investigations focus on steady crossflow modes as the primary disturbances. Upon downstream amplitude saturation, high-amplitude crossflow vortices oriented in streamwise direction are formed, which distort the flow field and cause strong shear layers that trigger a subsequent 'explosive' secondary instability mechanism, finally leading to laminar breakdown. Principally, three different classes of secondary instability modes were identified (the letter notation follows the suggestion of Malik *et al.* 1999): (i) The high-frequency 'mode I' or 'z' mode, induced by the minimum of the spanwise gradient of the streamwise velocity component, (ii) the high-frequency 'mode II' or 'y' mode, induced by the local maximum of the wall-normal gradient, and the low-frequency 'mode III', most likely linked to the maximum of the spanwise gradient. The modes exhibit their amplitude maxima in the respective regions of the deformed three-dimensional mean flow, i.e. the most amplified 'z' mode is located at the updraft crossflow vortex side, and the 'y' mode on top of the vortex. The weaker amplified mode-III class is found under the vortex close to the wall. The primary more unstable, unsteady CF disturbances have been found to be dominant at high freestream-turbulence conditions, where they are generated on higher amplitude levels and suppress the development of the unstable steady modes. The saturated travelling crossflow vortices give rise to a co-travelling secondary instability, not unlike the instability in the steady crossflow-vortex case described above, see, e.g. Wassermann & Kloker (2003).

The case of laminar flow throughout the FPG region and transition not before the APG region has been assumed to be rather unrealistic up to date, since early transition has always been observed on swept wings. However, recent work on transition control in three-dimensional crossflow dominated boundary-layer flows has proved the possibility of a significant delay in laminar breakdown, as discussed below.

Boundary-layer suction at the wall has long been considered as the appropriate method for transition delay on swept wings. Numerous investigations were performed on this topic, see the overview of Joslin (1998). Sometimes a significant delay in transition was obtained, although the nonlinear mechanisms arising from the distributed, discrete suction through wall porosities are not really understood yet (see, e.g.

Messing & Kloker 2003). A different method for transition delay on swept wings has been reported by Saric, Carrillo & Reibert (1998*a*), see also Saric *et al.* (2003), using the distributed roughness technique which is an upstream flow deformation (UFD) technique. The basic idea of this method is to directly influence the crossflow vortex modes most dangerous for triggering secondary instability by a technically simple technique, in which a spanwise row of artificial roughnesses is attached near the leading edge, with a roughness spacing smaller than the wavelength of the most amplified mode. By exciting an only weakly unstable crossflow vortex mode with comparably small spanwise wavelength, the naturally growing vortices are hindered in growth, and thus the onset of the secondary instability mechanisms is pushed downstream significantly. The effectiveness of the latter method has also been demonstrated in DNS investigations (Wassermann & Kloker 2002), elucidating the complex nonlinear mechanisms, necessary to understand the working of the UFD technique.

Based on the prospect of successful transition delay on swept wings, transition scenarios in the APG region come into the focus of interest. Considering this regime, typically TS-wave dominated transitions similar to regimes observed in two-dimensional boundary-layer flows are predicted. This prognosis is based only on the local primary instability properties of the flow, neglecting its streamwise parabolic characteristics. For example, the transition prediction strategy based on N_{CF} and N_{TS} factors is based on the same procedure (cf. Crouch & Ng 2002). The N-factors for CF modes and TS modes are calculated independently of each other based on the local stability properties of the undisturbed base flow, and subsequently transition is predicted to occur when the (N_{CF}, N_{TS}) combination exceeds a threshold curve in the (N_{CF}, N_{TS})-plane. The parabolic character of disturbance development, e.g. the presence of a persistent mean flow distortion, and the possibility of mode interaction, such as mutual suppression, is inherently neglected within this approach.

A first tentative investigation including the APG region of a generic three-dimensional base flow has been performed by Spalart (1993), using temporal DNS. The superimposed development of a steady CF mode and an unsteady TS wave was simulated for various amplitude ratios using a very coarse numerical resolution, based on fixed local base flow velocity profiles taken from different downstream positions. The idea was to abandon the (N_{CF}, N_{TS}) amplification plane and to use the physically more sound (M_{CF}, M_{TS}) amplitude plane, where M is the logarithm of the actual amplitudes. Transition was sensed by a drop of the shape factor H_{12} by -0.1, which, however, can also be induced by the sole large, possibly uncritical, steady vortex. The results indicate fundamental (K-type) breakdown if the weakly amplified CF vortex has a final amplitude of less than 3 %, because then the strongly amplified TS wave can grow over it and dominate. A completely unidentified scenario occurred for 4 % initial vortex amplitude, with dominated TS wave. The conclusion was '... that transition occurs when either instability mode becomes nonlinear, not when the product of their amplitudes reaches a threshold. At that point the (finally) weaker mode can trigger the secondary instability of the stronger one...', and therefore seemingly confirms the (N_{CF}, N_{TS})-strategy. Thus, as we understand it, the most likely situation in the APG region has not been clarified.

Chernoray *et al.* (2001) have experimentally studied the influence of a 30° sweep angle on K-breakdown in the APG region on a wing. Disturbances were triggered by roughness elements placed periodically along the spanwise direction at 30 % chord, and a single-frequency sound wave. They found that, in the swept case, no clear Λ-vortices appeared, and that 'there are two regions of high-shear layer along each (flow) structure. It can be concluded that, due to the crossflow, the temporal-spatial

structures ... over the swept wing have revealed significant differences in K-type transition to turbulence.'

Therefore, only the knowledge gained for transition in two-dimensional boundary-layer flows can provide some idea as to what can be expected in the APG region. There are two transition scenarios with steady modes involved: (i) The classical K-type transition is initiated by a large two-dimensional TS wave and a three-dimensional steady mode with smaller amplitude. When the TS wave surpasses the threshold amplitude of about 1 %, fundamental resonance occurs, and the lower-amplitude three-dimensional modes nonlinearly generated are strongly amplified, triggering the final breakdown (cf. Kachanov 1994; Bake, Meyer & Rist 2002). (ii) In the case of large-amplitude ($\geqslant 5-10$ %) steady modes in two-dimensional flows, typically streaks are observed. The streaks, having streamwise velocity disturbances similar to a vortex but with much less disturbance in the direction of the crosscut plane, form strong shear layers inside the boundary layer and when they surpass the threshold-amplitude of 26 %, they cause a strongly amplified inviscid secondary instability triggering the final breakdown (cf. Andersson *et al.* 2001). The most amplified secondary mode is found to be a sinuous mode of fundamental or subharmonic spanwise wavenumber depending on the streak amplitude. The sinuous mode is clearly connected to the region of maximal spanwise gradient of the steady deformed mean flow. The latter mechanism, a localized instability of strong shear layers formed by the primary disturbances, is similar to crossflow-induced transition or Görtler-vortex breakdown.

Since transition in the APG region of a swept wing becomes realistic only under special flow conditions, such as successful transition delay, two major types of transition regime turn out to be the most likely, depending on the flow conditions upstream. First, a scenario characterized by a successful UFD is conceivable. Former investigations (Saric *et al.* 1998*a*; Wassermann & Kloker 2002) have shown that it is possible to suppress transition throughout the FPG region by means of artificially superimposed small-wavelength CF vortices. Then, the latter are present with high-amplitude level ($\geqslant 10$ %) throughout the APG region. Secondly in the case of low-turbulence conditions and very smooth surface, or in the case of successful boundary-layer suction, the most amplified CF vortex modes may not exceed the threshold amplitude level necessary to trigger the onset of explosive secondary instabilities in the FPG region. Since former investigations have shown the persistent nature of crossflow vortices, finite-amplitude crossflow vortices remaining from upstream will always be present, and their spanwise wavenumber and amplitude level depend on the disturbance regime upstream. In any case, the crossflow vortices influence the further downstream development significantly. For the CF vortex modes, an amplitude level of at least 1–5 % seems to be reasonable in the situations discussed. Thus, standard K-type transition may be excluded in the APG region. Unsteady CF waves coming from upstream are damped in the APG region and cannot nonlinearly generate relevant TS waves, i.e. waves travelling in the direction of the streamline. Moreover, a (linear) changeover from CF- to TS-type disturbance has not been found, see Spalart (1993).

In this paper, we address the issue of breakdown mechanisms in the APG region of a swept wing, and also give some guidance for possibilities of (active) transition control in this regime. By means of spatial DNS of a generic three-dimensional boundary-layer flow with internal disturbance forcing, the following crucial points are tackled:

(i) Revision of the local and non-local primary instability properties of the base flow considered.

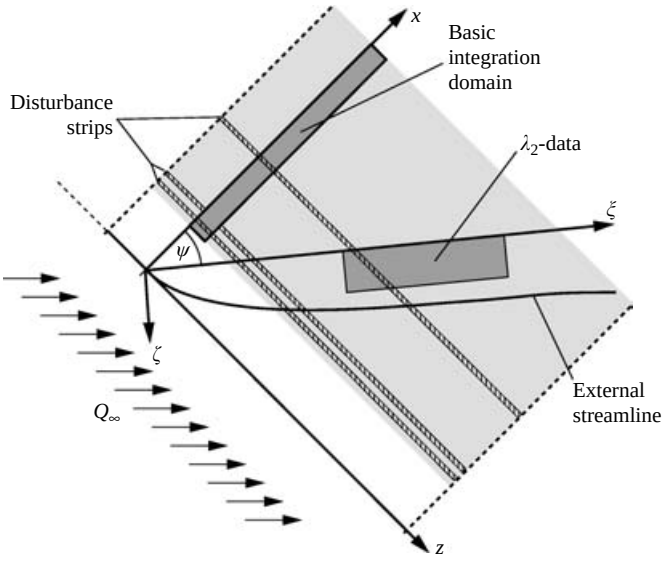

FIGURE 1. Top view of the swept flat plate with the vortex-oriented coordinate system (ξ, ζ), rotated by $\psi = 39^\circ$ versus the chordwise system (x, z).

(ii) Influence of crossflow vortices with various finite amplitudes and spanwise wavenumbers on the development of TS waves.

(iii) Examination of secondary instability mechanisms initiated by finite crossflow vortices in the APG region.

(iv) Extraction and comparison of the fundamental, subharmonic and detuned (with respect to the spanwise wavenumber of the primary disturbance) secondary instabilities.

(v) Visualization and identification of relevant flow structures during the breakdown stage.

(vi) Possibility of the effectiveness of a UFD even throughout the APG region (in a 'clean-condition' DNS).

The structure of the paper is as follows. In § 2, the numerical method is briefly described; § 3 outlines the used baseflow, and in § 4, its primary instability properties are discussed. In § 5, the main results for three different primary vortex states are presented.

2. Numerical method

2.1. *Governing equations and discretization*

The numerical method for spatial DNS is based on a vorticity–velocity formulation. All variables are non-dimensionalized by the reference length $\bar{L} = 0.05\,\mathrm{m}$, and the chordwise free-stream velocity $\bar{U}_\infty = 30\ \mathrm{m\ s^{-1}}$. The global reference Reynolds number is $Re = \bar{U}_\infty \bar{L}/\bar{\nu} = 100\,000$, where the overbar denotes dimensional variables and $\bar{\nu}$ is the kinematic viscosity.

We have the vectors of vorticity $\boldsymbol{\omega} = \{\omega_x, \omega_y, \omega_z\}^T$ and velocity $\boldsymbol{u} = \{u, v, w\}^T$, with the first component in the chordwise (x-), the second component in the wall-normal (y-) and the third component in spanwise (z-) direction (figure 1). The vorticity

components are defined as

$$\omega_x = \frac{\partial v}{\partial z} - \frac{\partial w}{\partial y}, \quad \omega_y = \frac{\partial w}{\partial x} - \frac{\partial u}{\partial z}, \quad \omega_z = \frac{\partial u}{\partial y} - \frac{\partial v}{\partial x}. \tag{2.1}$$

We use a disturbance formulation keeping the full equation set, in order to ease formulation of boundary conditions. For the calculation of the disturbance quantities, the assumption of infinite span yields periodic boundary conditions in the spanwise direction. Thus, the numerical method uses a complex Fourier spectral representation in the spanwise direction to calculate the non-symmetric three-dimensional flow. The discrete waves are presented in the frequency–spanwise wavenumber spectrum (h, k), so the mode (h, k) denotes a mode with the frequency $h\beta_1$ and the spanwise wavenumber $k\gamma_1$. In the x- and y-directions, a compact finite-difference (FD) discretization of sixth order is used, based on a blockwise equidistant rectangular grid with a special wall zone, where the step size Δy is halved. The time integration is done by a four-step fourth-order Runge–Kutta method.

Defined disturbances are introduced in the laminar flow field in several disturbance strips at the wall where the disturbances are enforced with momentum input, but no net mass flow, using blowing and suction:

$$v'(x, y, z, t) = f_v(x)\left(\sum_{k=1}^{K} 2A_{0,k}\cos(k\gamma z + \Theta_{0,k}) + \sum_{h=1}^{H}\sum_{k=-K}^{K} 2A_{h,k}\cos(k\gamma z - h\beta t + \Theta_{h,k})\right);$$

$f_v(x)$ is a fourth-order parabola with zero values, and zero first and second x-derivatives at its ends of the respective strip. For a detailed description of the numerical method see Wassermann & Kloker (2002), and for a further validation also Saric *et al.* (2003).

2.2. *Numerical parameters*

For the simulations, the uniform blockwise equidistant grid typically contained 257 points in the wall-normal direction, for the first 33 points $\Delta y_{wz} = \Delta y/2$, $\Delta y = 0.000278$. In the x-direction, between 1826 and 2626 points were used with $\Delta x = 0.0017952$, depending on the downstream extent of the integration domain; the time step was $\Delta t = 0.000393$ corresponding to approximately half the maximum value given by the viscous stability limit near the wall. In the spanwise direction, the highest mode considered typically has $\gamma_{max} = 720$, but for the high-resolution calculations of the late stages of transition even $\gamma_{max} = 1440$, corresponding to 32 de-aliased spanwise modes, is considered. For the sake of consistent mode labelling, the (h, k)-notation used corresponds to a basic spanwise wavenumber of $\gamma_1 = 45.0$, independent of the computational spanwise wavenumber γ_c used for the current simulation, i.e. in some simulations $\gamma_c = 22.5$ resulting in the occurrence of modes $(h, 0.5)$, $(h, 1.5)$ etc. In other simulations $\gamma_c = 90.0$, i.e. only the modes $k = 0, 2, 4, 6, \ldots$ are calculated. The fundamental frequency corresponding to $h = 1$ is not the same throughout the simulations. In the simulations dealing with TS-instabilities, the fundamental frequency is $\beta = 16$, whereas it is $\beta = 10$ in the cases with the background pulses inducing high-frequency secondary instabilities. All relevant simulation parameters are summarized in table 1. In former investigations, it has been shown that the typical grid used with γ_{max} eight times the spanwise wavenumber of the dominating primary mode is fine enough to capture correctly the investigated flow physics.

Case	Primary disturbances	Additional disturbances
TSW	$\beta = 16;\ \gamma = 21;\ x_d = 2.0;\ A = 10^{-6}$	
CFW	$\beta = 14;\ \gamma = 90;\ x_d = 0.68;\ A = 10^{-6}$	
CFV-low	$\beta = 0;\ \gamma = 90;\ x_d = 0.68;\ A = 0.0002$	
CFV-low/TS-low	$\beta = 0;\ \gamma = 90;\ x_d = 0.68;\ A = 0.0002$	$\beta = 16.0;\ \gamma = \pm 22.5;\ x_d = 2.0;$ $A = 1.0 \times 10^{-5}$
CFV-low/TS-med	$\beta = 0;\ \gamma = 90;\ x_d = 0.68;\ A = 0.0002$	$\beta = 16.0;\ \gamma = 22.5;\ x_d = 2.0;$ $A = 0.002$
CFV-med	$\beta = 0;\ \gamma = 90;\ x_d = 0.68;\ A = 0.001$	
CFV-med/TS-low	$\beta = 0;\ \gamma = 90;\ x_d = 0.68;\ A = 0.001$	$\beta = 16.0;\ \gamma = \pm 22.5;\ x_d = 2.0;$ $A = 1.0 \times 10^{-5}$
CFV-med/pulses	$\beta = 0;\ \gamma = 90;\ x_d = 0.68;\ A = 0.001$	Periodic background pulses: $x_d = 2.0, 2.5, 3.0, 3.5$ $\beta = 10 - 300,\ \Delta\beta = 10;$ $\gamma = \pm 22.5, \pm 45.0, \pm 90.0$
CFV-med/pulsed	$\beta = 0;\ \gamma = 90;\ x_d = 0.68;\ A = 0.001$ $\Delta x, \Delta y$ refined	Periodic background pulses: $x_d = 3.5$ $\beta = 10 - 300,\ \Delta\beta = 10;\ \gamma = \pm 90.0$
UFD-high	$\beta = 0;\ \gamma = 45, 90, 135, 180;$ $x_d = 0.68;\ A = 0.005$ UFD: $\beta = 0;\ \gamma = 135;\ x_d = 0.57;$ $A = 0.05$	
UFD-high/pulses	$\beta = 0;\ \gamma = 45, 90, 135, 180;$ $x_d = 0.68;\ A = 0.005$ UFD: $\beta = 0;\ \gamma = 135;\ x_d = 0.57;$ $A = 0.05$	Periodic background pulses: $x_d = 2.5, 3.0, 3.5$ $\beta = 10 - 300,\ \Delta\beta = 10;$ $\gamma = \pm 22.5, \pm 45.0, \pm 90.0$

TABLE 1. Simulation cases.

3. Laminar base flow

The base flow is designed to model the basic flow characteristics on the suction side of a swept wing, with decreasingly favourable pressure gradient followed by an adverse pressure gradient. The streamwise edge velocity is adopted from Spalart, Crouch & Ng (1994) and defined analytically by

$$u_{p0}(x) = \frac{3}{2\pi}\left(\arctan\left(\frac{x-a}{b}\right) + \arctan\left(\frac{x+a}{b}\right)\right) - cx \tag{3.1}$$

$$\text{with} \quad a = 0.2611, \quad b = 0.41015, \quad c = 0.056.$$

The integration domain starts at $x_0 = 0.25$ close to the leading edge (local Hartree $\beta_H(x_0) = 0.99$) and extends up to $x_N = 4.96$. The sweep angle is $\varphi_\infty = 45^\circ$ and the local angle of the external streamline varies from $\varphi_e(x_0) = 68.1^\circ$ to the minimum value of $\varphi_e = 39.7^\circ$ at $x = 2.65$ and $\varphi_e(x_N) = 41.1^\circ$ (figure 2). The crossflow profiles at various downstream positions are shown in figure 3. In the region of favourable pressure gradient (FPG) there is a distinct crossflow component inside the boundary layer towards the center of curvature. The maximum crossflow amplitude $\tilde{w}_{s,B} = w_{s,B}/u_{s,B,e}$ is about 20 % at $x = 0.4$ and decreases monotonously downstream up to $x = 4.4$; in the APG region, the crossflow amplitude remains at about 3 %. The direction of the crossflow near the wall changes sign at $x = 3.44$, and downstream the crossflow profiles $w_{s,B}(y)$ are s-shaped. The streamwise profile $u_{s,B}(y)$ shows the FPG-shape in the front region and becomes inflectional downstream at $x \approx 2.8$. The chordwise

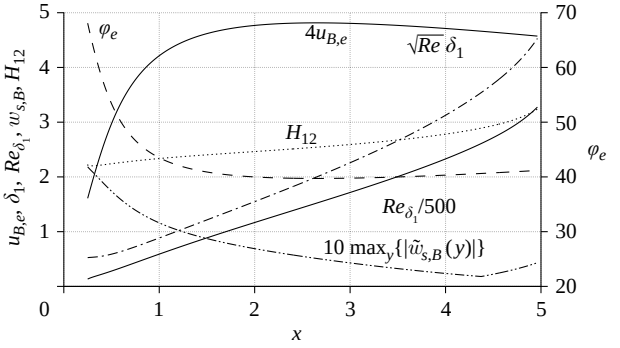

FIGURE 2. Base flow parameters in the plate-fixed coordinate system.

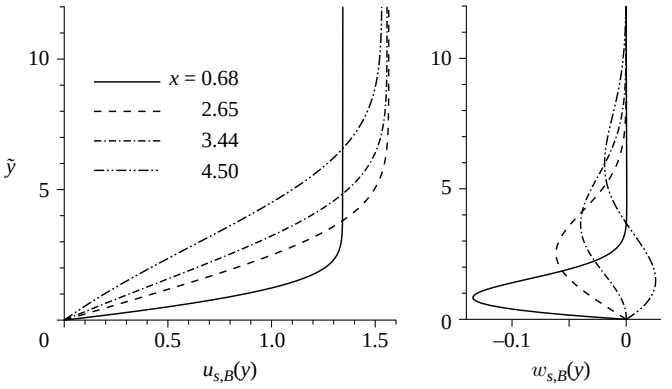

FIGURE 3. Mean flow and crossflow profiles at various downstream positions; $\tilde{y} = \sqrt{Re}\,y$.

shape parameter H_{12} increases monotonously downstream up to 3.0 corresponding to a Hartree parameter of $\beta_H = -0.15$.

4. Primary instability properties

The base flow has been thoroughly analysed by means of spatial linear stability theory to form an overview of relevant instability modes. The local linear analysis shows that the stability characteristics of the flow are significantly changing downstream with altering pressure gradient. First, crossflow instability is clearly dominating with wave vectors of the most unstable modes nearly perpendicular to the inviscid streamline ($\gamma_s \gg \alpha_{r,s}$, γ_s, $\alpha_{r,s}$ denote the spanwise and streamwise wavenumber in the streamwise coordinate system, respectively). The instability domain in the (γ_s, $\alpha_{r,s}$)-plane is asymmetric with significantly stronger amplification for the waves travelling against the crossflow (figure 4*a*, *b*). Further downstream, in the APG region, TS instability becomes dominant, with wave vectors of the most unstable modes nearly parallel to the inviscid streamline, $\gamma_s \ll \alpha_{r,s}$. The local instability region in the (γ_s, $\alpha_{r,s}$)-plane consists of a CF instability part and the clearly dominating, roughly symmetric TS part (figure 4*c*, *d*).

The steady CF modes are partly amplified throughout the whole integration domain (figure 5*a*) suggesting that these modes will play a significant role in the APG region as well. The amplification for unsteady CF waves travelling with the crossflow ($\gamma_s < 0$)

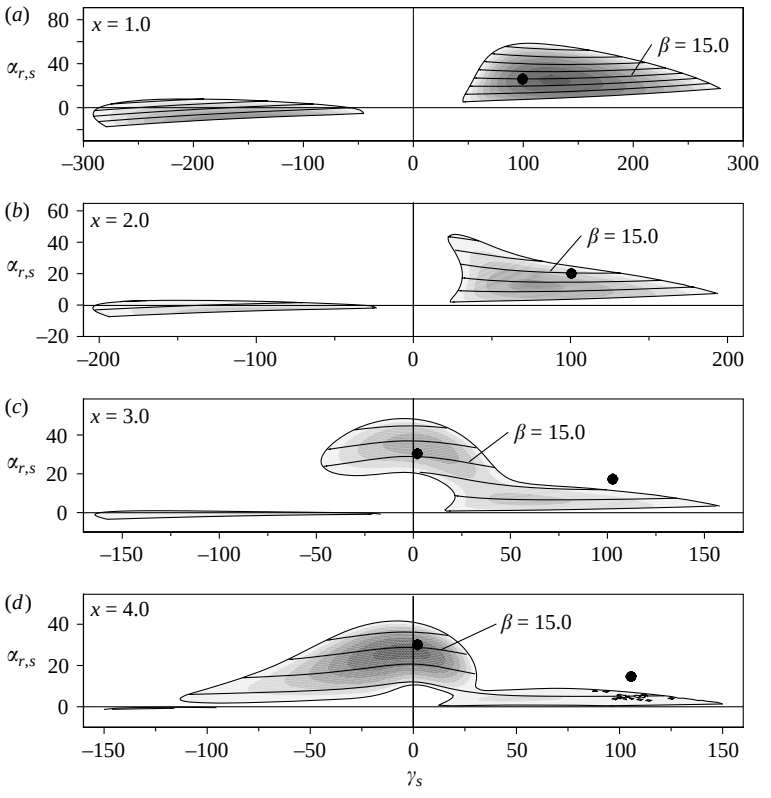

FIGURE 4. Spatial amplification rate α_i (shaded) as obtained from linear stability theory in the streamline coordinate system (γ_s, $\alpha_{r,s}$) at four equidistant downstream positions (note the different range for $\alpha_{r,s}$ and γ_s in the various subfigures). $\alpha_i \leqslant 0$; $\Delta\alpha_i = 0.5$; $\Delta\beta = 5.0$. The outer isoline denotes the neutral curve. Additionally, curves of constant frequency are shown, the curve for $\beta = 15$ especially marked. The frequency increases with increasing $\alpha_{r,s}$. The dots mark the CF-mode considered in case CFW and the TS-mode considered in case TSW, respectively.

strongly attenuates with increasing frequency, and the instability domain for unsteady ($\gamma_s \gg 0$)-CF-waves concentrates in the FPG region. For the higher frequencies ($\beta = 16$), a second instability region can be detected downstream of $x = 2.2$ representing the TS instability in the APG region (figure 5*b*).

Two simulations have been performed considering the quasilinear downstream development of a representative CF wave and a representative TS wave. In case CFW, the CF mode with $\beta = 14$ and $\gamma = 90$ has been introduced at $x = 0.68$, whereas in case TSW, the TS mode with $\beta = 16$ and $\gamma = 21$ has been excited at $x = 2.0$. Figure 6 shows a comparison of the amplitude development and the spanwise wavenumbers, respectively. The CF mode is strongly amplified first and damped as soon as the pressure gradient changes sign. The TS mode, on the other hand, is damped first and does not grow until the pressure gradient becomes adverse. The spanwise wavenumber varies only slightly downstream for both modes; thus the CF mode wave vector encloses an angle of about 80° with the inviscid streamline, whereas the wave vector of the TS mode is aligned with an angle of only about 5°. Simulations of modes with identical spanwise wavenumber and frequency, but different disturbance strip position clearly showed that they keep their characteristics downstream, i.e. no mode changeover was observed. Initiated in the FPG region, (CF) amplitude decay occurred

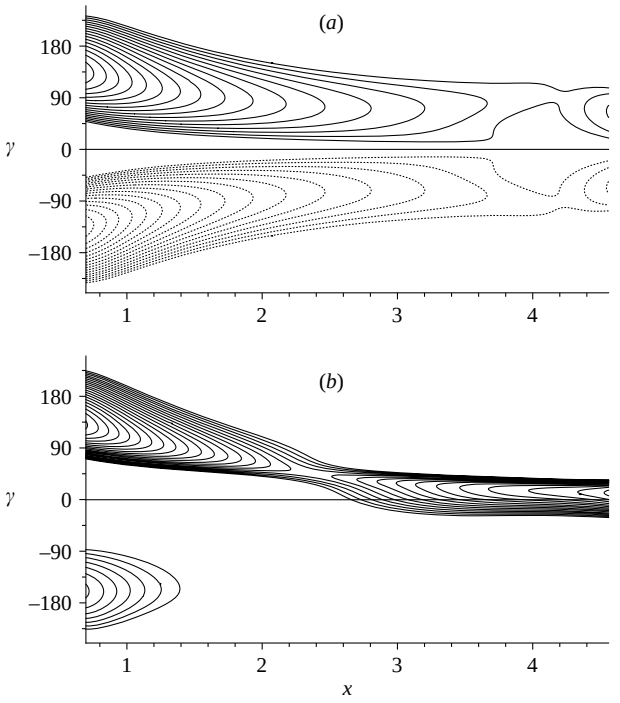

FIGURE 5. Stability diagram from LST for (*a*) $\beta = 0$ and (*b*) $\beta = 16$. $\alpha_i \leqslant 0$; $\Delta\alpha_i = 0.25$.

in the APG region at $x = x_s$, whereas the initiation in the APG region yielded (TS) growth at $x = x_s$ (see also Spalart *et al.* 1994).

5. Investigation of transition mechanisms

If laminar breakdown has not occurred in the FPG region, transition scenarios with finite-amplitude steady CF vortices remaining from upstream are realistic; the amplitudes of the CF modes are then just lower than the threshold levels for secondary instability in the FPG region. This holds for a smooth surface, or for successful control of the CF instability process by means of suction panels or the UFD technique.

5.1. *The steady primary states*

We have considered three main scenarios for the following clarification of transition mechanisms in the APG region. First, we investigate two cases with a finite-amplitude steady CF mode with the naturally most amplified spanwise wavelength (cases CFV-low and CFV-med). This mode has been excited far upstream with two different amplitudes, but in either case, small enough to prevent onset of secondary instability in the FPG region. The third scenario (UFD-high) mimics a successful delay of transition by means of an upstream flow deformation, as investigated in detail in our previous paper Wassermann & Kloker (2002). Here, the dominating steady CF mode has a subcritical spanwise wavelength and suppresses the natural transition process in the FPG region typically triggered by secondary instability.

In case CFV-low, the steady mode $(0, 2)$, $\gamma = 90$ has been introduced at $x = 0.68$ with an amplitude of $A_{(0,2)} = 0.0002$. Owing to the low excitation amplitude, the mode develops quasi-linearly throughout the whole integration domain (figure 7*a*). The

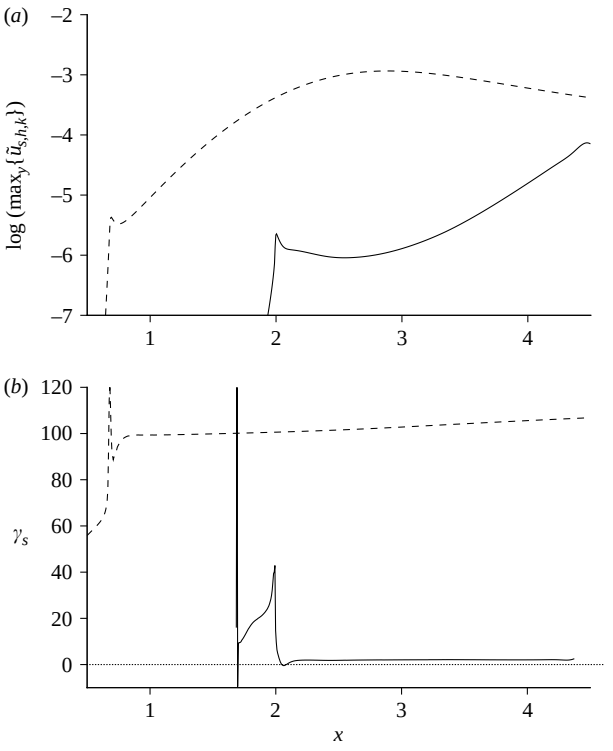

FIGURE 6. Comparison of the quasi-linear amplitude development and the spanwise wavenumber of - - -, a typical CF-wave (case CFW, $\beta = 14$, $\gamma = 90$) and —, a typical TS-Wave (case TSW, $\beta = 16$, $\gamma = 21$).

mode is strongly amplified first, and the growth continues in the APG region. The mode attains a maximal amplitude of 12.5 % at $x = 4.5$. The nonlinearly generated higher harmonics (modes (0, 4), (0, 6), (0, 8), etc.) play a minor role. At $x = 3.5$, the amplitudes are approximately 0.5 %, 0.05 % and 0.005 %, i.e. the saturated steady state can be mainly described by only the fundamental mode (0, 2), attaining an amplitude of 7.0 % at this position. This is important concerning the shape of possible secondary instability modes.

In case CFV-med the mode (0, 2) has been introduced with an amplitude five times higher. The mode is strongly amplified by primary instability, not surpassing the threshold amplitude for secondary instability in the FPG region (figure 7*b*). The amplitude growth differs from the quasilinear development downstream of $x \approx 2.3$ and eventually saturates. The $\tilde{\omega}_{x,s}$-component saturates at $x \approx 3.3$ (the far-wall maximum of $\tilde{\omega}_{x,s}(y)$ is traced), whereas the $\tilde{u}_s$-component grows up to $x \approx 4.1$, attaining a modal amplitude of 33 %. The different saturation locations are due to the integral effect of the vortical motion on the streamwise disturbance. The nonlinearly generated higher harmonics cannot be neglected any more. At $x = 3.5$, their amplitudes are approximately 7.2 %, 2.5 % and 0.07 % compared to 27.7 % for the fundamental mode (0, 2). Thus, all modes are necessary to describe the nonlinear saturated state.

In physical space, streamwise vortices establish with clockwise rotation when looking downstream. The vortices transport slow fluid from the near-wall region up into faster regions and vice versa, resulting in a u'_s-disturbance that grows further on, even when the vorticity is already decaying. The initiated steady deformation of

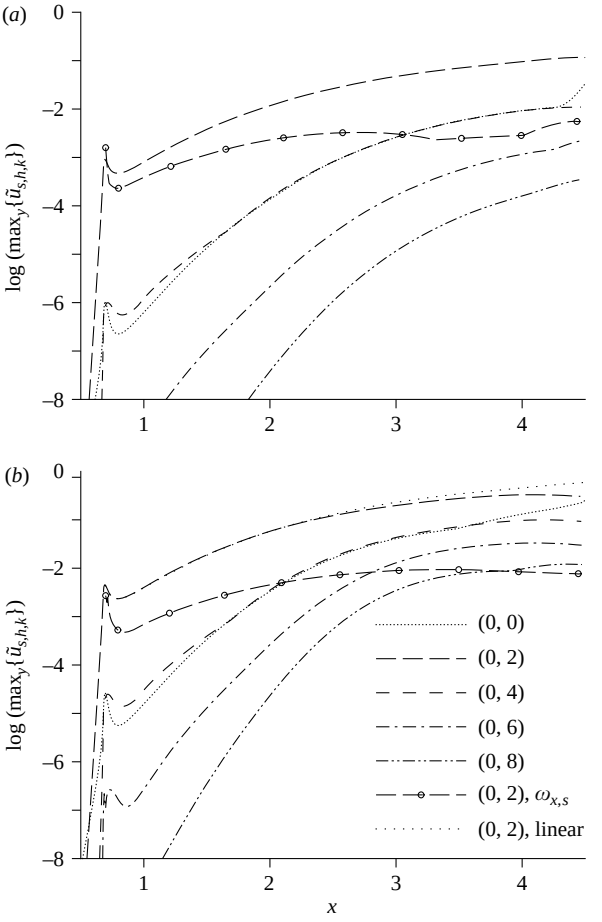

FIGURE 7. Downstream (t-z)-modal amplitude development for (a) case CFV-low and (b) case CFV-med; $\tilde{u}_{s,h,k}$-maximum over y, $\tilde{u}_s = u_s/u_{s,B,e}$.

the mean flow is shown in figure 8 (case CFV-low) and figure 9, left (case CFV-med) in a crosscut in the vortex-oriented coordinate system (ξ, ζ) (cf. figure 1) far downstream in the APG region. Owing to the low disturbance amplitude in case CFV-low the deformation is rather weak. The deformed mean flow $\langle u_s \rangle$ shows only a weak undulation resulting in very small gradients $\langle \partial u_s/\partial y \rangle$, $\langle \partial u_s/\partial z \rangle$. In case CFV-med, local regions of clearly accelerated and decelerated mean flow alternate, and strong shear layers are formed inside and at the edge of the boundary layer. The region of large y-gradient (figure 9d) extends relatively far away from the wall. Figure 9(e) uncovers a second counter-rotating vortex, situated on the left-hand side of the primary vortex somewhat closer to the wall. Therefore, compared to a saturated vortex in the FPG region (figure 9, right), the main shear layer is lifted up. Thus the shear layer caused by the positive z-gradient of $\langle u_s \rangle$ is now stronger than that caused by the negative gradient in the updraught region. Since the direction of the crossflow has changed sign in the near-wall region, the deformation of the flow is somewhat distorted in the positive ζ-direction here.

In case UFD-high, the basic disturbance to be suppressed is a vortex-mode packet (modes (0, 1)–(0, 4)), excited at $x = 0.68$ with an amplitude of $A_{(0,k)} = 0.005$ for each

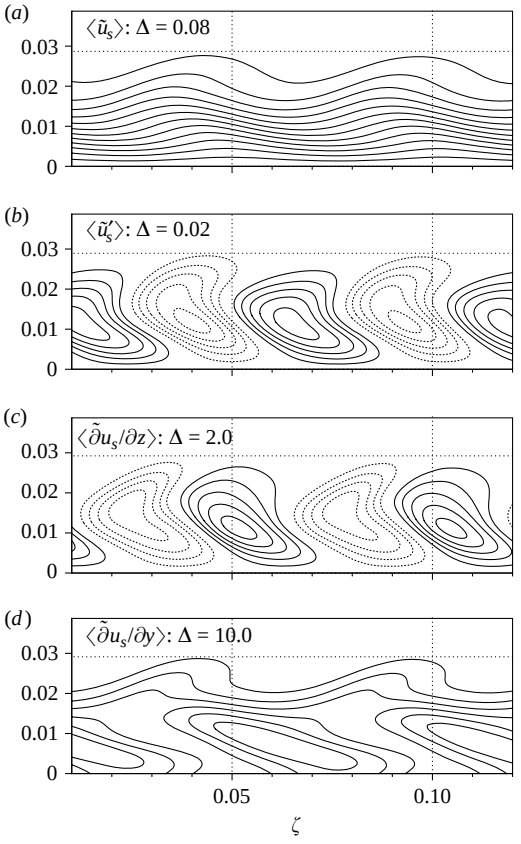

FIGURE 8. Flow field distorted by the nonlinearly saturated crossflow vortex mode (case CFV-low) in a cross-section in the vortex-oriented system at $\xi = 5.5$ ($\zeta = 0 \rightarrow x = 4.27$): (*a*) deformed mean flow; (*b*) deformation of the mean flow; (*c*), (*d*) z- and y-gradient of the deformed mean flow. Positive isolines are solid; negative isolines are dotted. The zero line is not shown. To scale. The dotted horizontal line markes the laminar boundary-layer thickness at $\zeta = 0$. This quantity varies by only 2 % over the ζ-range shown here.

component. Additionally, the UFD mode (0, 3) has been forced at $x = 0.57$ with an amplitude of 5 % to suppress the growth of the other crossflow-vortex modes (figure 10). As shown in previous work (Wassermann & Kloker 2002) the resulting saturated steady state turns out to be secondarily stable in the FPG region. Owing to the dominance of the mode (0, 3), streamwise vortices establish with a spanwise spacing 2/3 of the spacing in case CFV-med. The flow deformation is much weaker than in case CFV-med and the shear layers are less pronounced (figure 11).

5.2. *Influence of finite-amplitude CF vortices on instability*

The first step for the following investigations is to clarify the influence of the three-dimensional flow deformation on the onset and amplification of TS instabilities. For the undisturbed base flow, local linear stability theory yields significant TS instability downstream of $x = 2.4$. To clarify the modified TS instability properties of the deformed mean flow in case CFV-low and in case CFV-med, the TS waves $(1, \pm 0.5)$ with $\beta = 16$, $\gamma = \pm 22.5$ have been additionally forced at $x = 2.0$ (cases CFV-low/TS-low and CFV-med/TS-low, respectively).

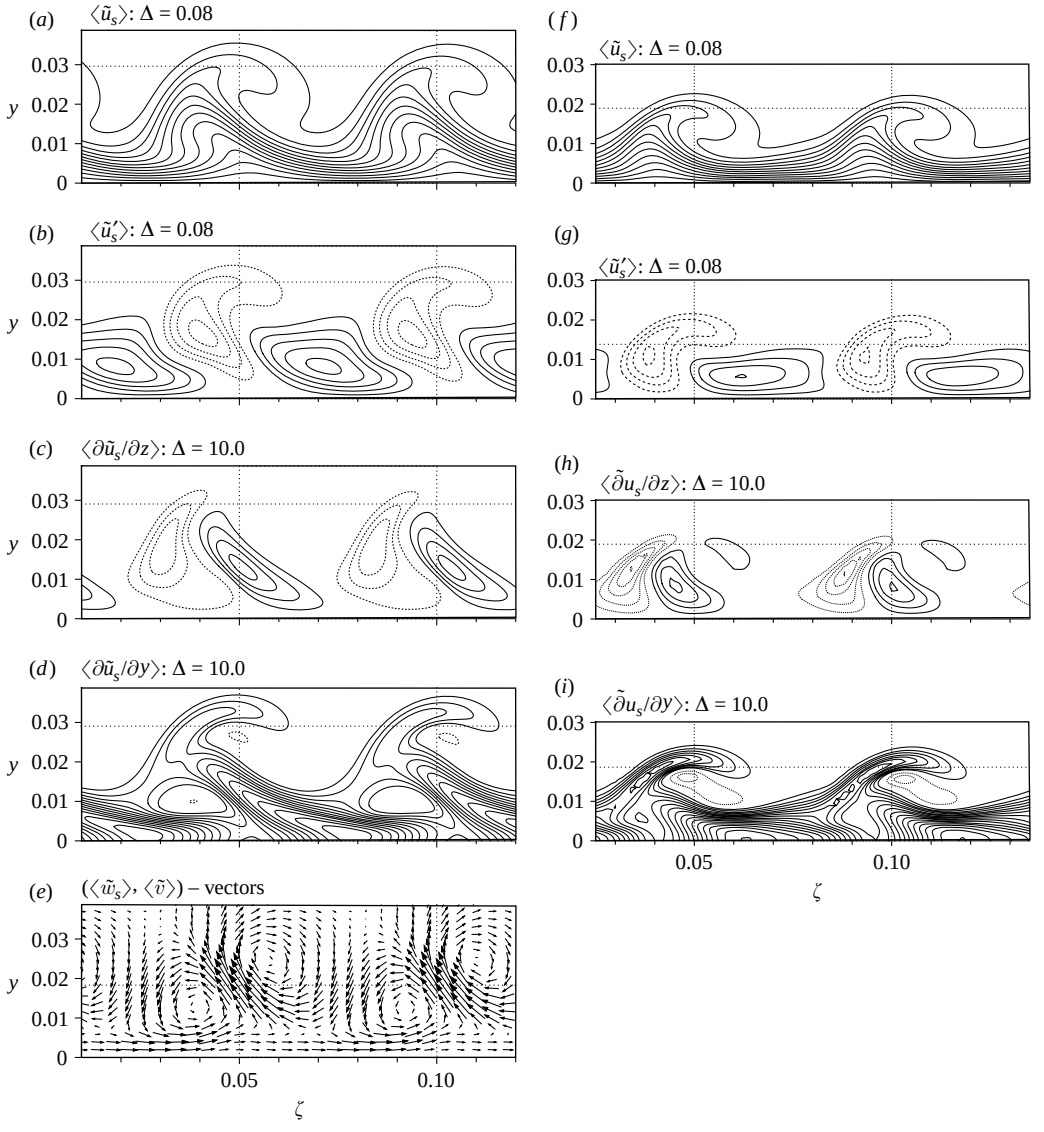

FIGURE 9. Left: as figure 8 but for case CFV-med. Right: corresponding flow field distorted by the nonlinearly saturated CF mode in the FPG region (for comparison, case 3 in Wassermann & Kloker 2002) in a cross-section in the vortex-oriented system at $\xi = 3.2$. (*e*) additionally shows the $(\langle\tilde{w}_s\rangle, \langle\tilde{v}\rangle)$ – vectors in the cross-section.

The amplitude plot for case CFV-low/TS-low, figure 12, shows that the growing of the TS wave $(1, 0.5)$ does not differ significantly from case TSW, although a comparison of the streamwise disturbance profiles (not shown) reveals some nonlinear effects. The modes $(1, 2.5)$ and $(1\,, -1.5)$ are initially nonlinearly generated by the TS wave together with the dominating vortex mode $(0, 2)$, but are significantly more strongly amplified than the TS wave, although LST predicts them to be damped. A short distance downstream, these modes already grow persistently and finally overtake the TS wave in amplitude. They represent a pair of oblique waves developing symmetrically with respect to the direction of the crests of mode $(0, 2)$ (see the sketch

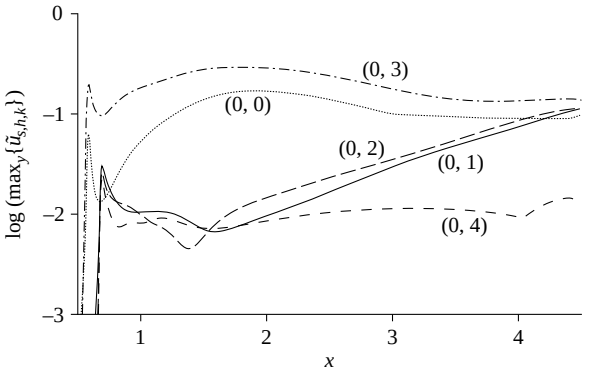

FIGURE 10. Downstream (t-z)-modal amplitude development in case UFD-high; CF vortex mode packet $(0, k)$, $k = 1 - 4$, plus UFD $(0, 3)$; $\tilde{u}_{s,h,k}$-maximum over y, $\tilde{u}_s = u_s/u_{s,B,e}$.

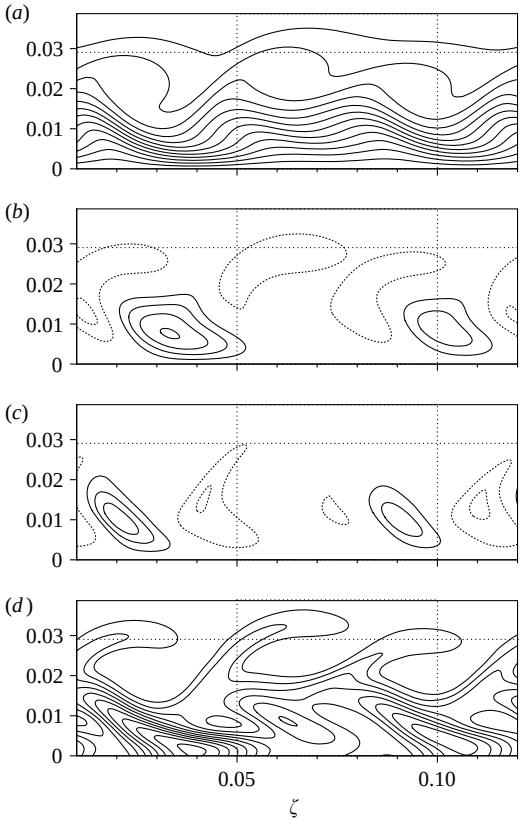

FIGURE 11. As figure 8, but for case UFD-high. (*a*) $\langle \bar{u}_s \rangle$: $\Delta = 0.08$; (*b*) $\langle \bar{u}_s' \rangle$: $\Delta = 0.08$; (*c*) $\langle \bar{\partial} u_s/\partial z \rangle$: $\Delta = 10.0$; (*d*) $\langle \bar{\partial} u_s/\partial y \rangle$: $\Delta = 10.0$.

in figure 13). In fact, they form a low-frequency secondary-instability mode of the deformed primary state that travels in the direction of the vortex mode crest. Since the amplitude of the primary mode is small, the primary state can be represented roughly by a single mode only (cf. figure 7*a*) and so can the secondary instability. The pair (1, 4.5) and (1, −3.5) generated by (0, 4) and the TS wave is an order of

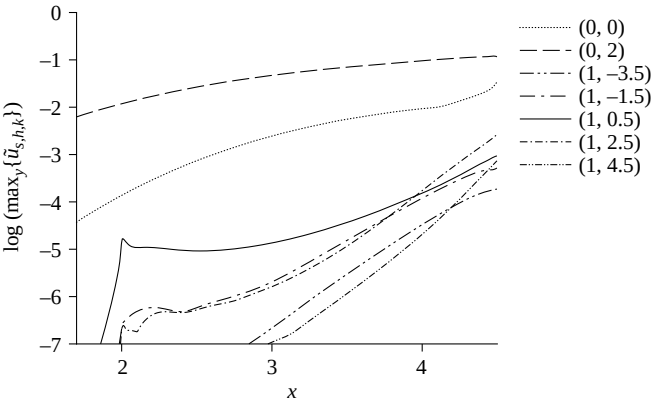

FIGURE 12. Downstream (t-z)-modal amplitude development in case CFV-low/TS-low; $\tilde{u}_{s,h,k}$-maximum over y, $\tilde{u}_s = u_s/u_{s,B,e}$.

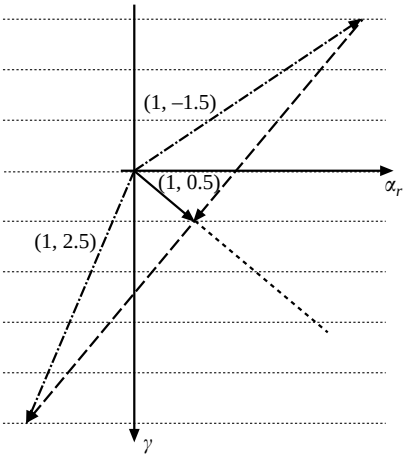

FIGURE 13. Wave vectors in case CFV-low/TS-low.

Mode	$\alpha_{r,s}$	γ_s
(0, 2)	1.7	116.2
(1, 2.5)	31.8	120.4
(1, −1.5)	29.2	−112.8

TABLE 2. Wavenumbers for the modes involved in case CFV-low/TS-low at $x = 3.5$. The wavenumbers for the various modes are calculated at the corresponding y-position of maximal amplitude.

magnitude smaller than the modes discussed. The symmetry of the pair of waves is sketched in figure 13 and can also be derived from table 2, where the wavenumbers are given in the streamline system.

In an additional simulation the direct excitation of the modes (1, 2.5) and (1, −1.5) does not yield the amplification found in case CFV-low/TS-low directly, since the modes forced in the disturbance strip at the wall differ in the streamwise wavenumber $\alpha_{r,s}$ at first. Not until $x \approx 3.7$ are the modes modulated and show the expected

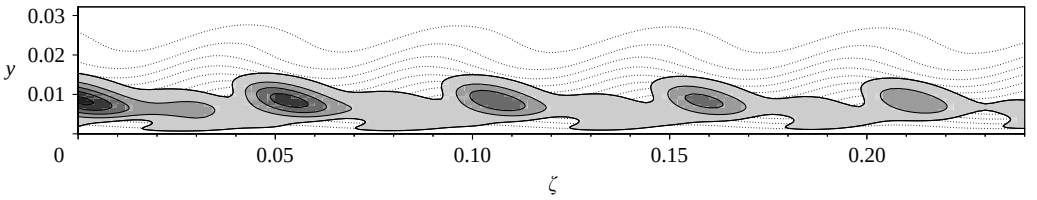

FIGURE 14. Isocontours of normalized $\tilde{u}_{s,h}$-amplitude in a cross-section in the vortex-oriented system for $\beta = 16$ at $\xi = 5.5$ for case CFV-low/TS-low. Isolines from 0.15 to 0.95 with a 0.2 spacing are shown and the deformed mean flow is indicated by the dotted lines.

behaviour. Thus, the excitation of the TS wave (1, 0.5) can be viewed as a near-optimal forcing to generate the secondary-instability mode since this way the transient region for the low-frequency secondary instability is minimal. That is, the TS wave itself plays no major role, but acts as accelerator in initiating low-frequency secondary instabilities. This is in contrast to K-breakdown. Figure 14 shows the t-modal amplitude distribution in a cross-section perpendicular to the crests of mode (0, 2). The region of maximal amplitude is situated between the regions of local acceleration and local deceleration, exactly at the position of maximal spanwise gradient $\langle \partial u_s / \partial z \rangle$. Hence it is a low-frequency 'z' mode.

For the forced mode (1, -0.5) and the nonlinearly generated pair of modes (1, -2.5) and (1, 1.5) no significant amplification can be found. Therefore these modes do not play any role in case CFV-low/TS-low.

In the case CFV-med/TS-low (figure 15) the growing of the mode (1, 0.5) differs somewhat more from case TSW, and can be interpreted as follows. First, a weakened TS amplification caused by the vortex mode is present ($x \leqslant 3.6$), see also Cossu & Brandt (2002), before the mode grows, since it is involved in an amplified low-frequency secondary instability ($x > 3.6$). The oblique waves (1, 2.5) and (1, -1.5) are generated on a higher level compared to case CFV-low. Subsequently, they are growing slightly more strongly than the TS wave, until at $x = 3.7$ the growth is almost the same for all modes, indicating the onset of a secondary instability. Owing to the fully nonlinear primary state in this case, the full spanwise spectrum is necessary to represent it, and so it is for the secondary instability. All the spectral modes shown in figure 15 are growing similarly, but now within a more equalized amplitude band compared to the previous case. They compose the low-frequency secondary instability, which is clearly more localized in physical space compared to case CFV-low/TS-low (figure 16*a*). Additionally to the TS mode (1, 0.5) the mode (1, -0.5) has been introduced by making the disturbance z-symmetric within the disturbance strip. As a result, the oblique modes (1, 1.5) and (1, -2.5) etc. are nonlinearly generated by the primary state. Figure 15*b* reveals that these modes finally grow like the ones discussed before, at approximately equal amplitudes (of figure 15*a*). In the framework of secondary instability theory these disturbances represent a (spanwise) detuned subharmonic mode, being virtually identical to the fundamental mode but with a phase shift of π at neighbouring vortices. The investigation of these detuned modes becomes possible since in this special calculation the spanwise wavenumber γ_f of the primary disturbance, the crossflow vortex mode, is four times the computational wavenumber γ_c. Formally, the various modes compose in the following way:

$$\hat{f}_{h,\delta}(x, y, z) = \sum_{k=-K/4}^{K/4} \hat{f}_{h,4(k+\delta)}(x, y) \exp(\mathrm{i}(k + \delta)\gamma_f z) \tag{5.1}$$

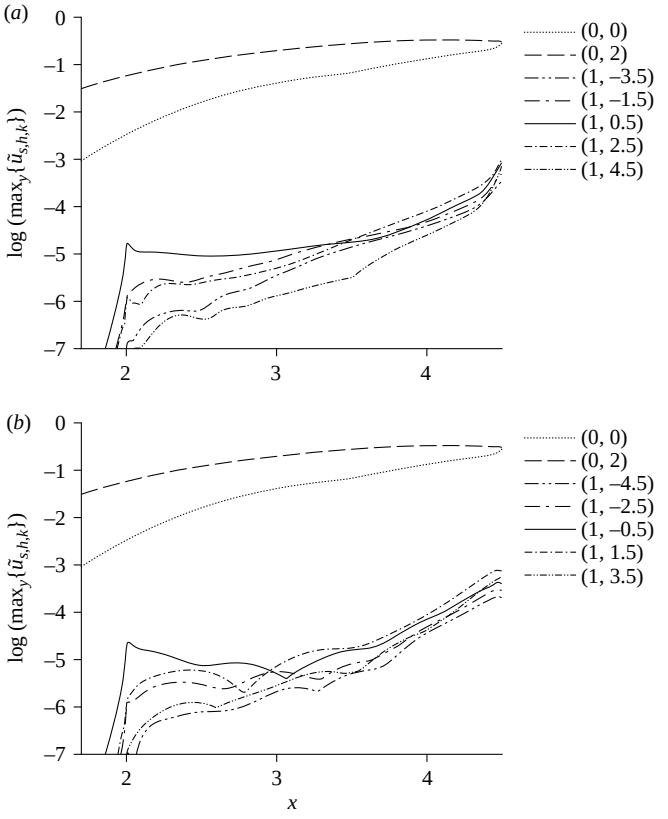

FIGURE 15. Downstream (t-z)-modal amplitude development in case CFV-med/TS-low; $\tilde{u}_{s,h,k}$-maximum over y, $\tilde{u}_s = u_s/u_{s,B,e}$.

where δ denotes the detuning parameter. With the computational raster used here, principally the detuning parameters $\delta = 0.0$, 0.25, 0.5 and 0.75 can be considered.

The two-dimensional amplitude distribution for the subharmonic mode looks like that for the fundamental mode (figure 16), and the superposition with approximately equal amplitude yields cancellation of secondary action at each second vortex. However, this situation can only occur for perfectly and uniformly distributed primary vortices. In general, the secondary instability occurs locally, if the shear layers are strong enough (see also Wassermann & Kloker 2002). In the 'perfect' case, it strongly depends on the initialization of the secondary instabilities. Typically, secondary action at any primary vortex will occur, possibly with some repeating phase shift in the streamwise direction from vortex to vortex.

In this context, a discussion of instability notation is due. A TS wave is a streamwise (and spanwise) and timewise harmonic disturbance, and it can be extracted from the flow field by means of a t-z-modal decomposition. Typically, a TS wave develops in a clean or only slightly disturbed two-dimensional base flow. In the case of a strongly deformed basic state it seems inappropriate to use the phrase '(localized) TS amplification' to describe the growth of any unsteady disturbance. In such cases, localized (secondary) amplification caused by the deformed primary state can be observed, and the development of the disturbances can be clearly characterized by their two-dimensional wall-normal–spanwise amplitude distribution and the streamwise

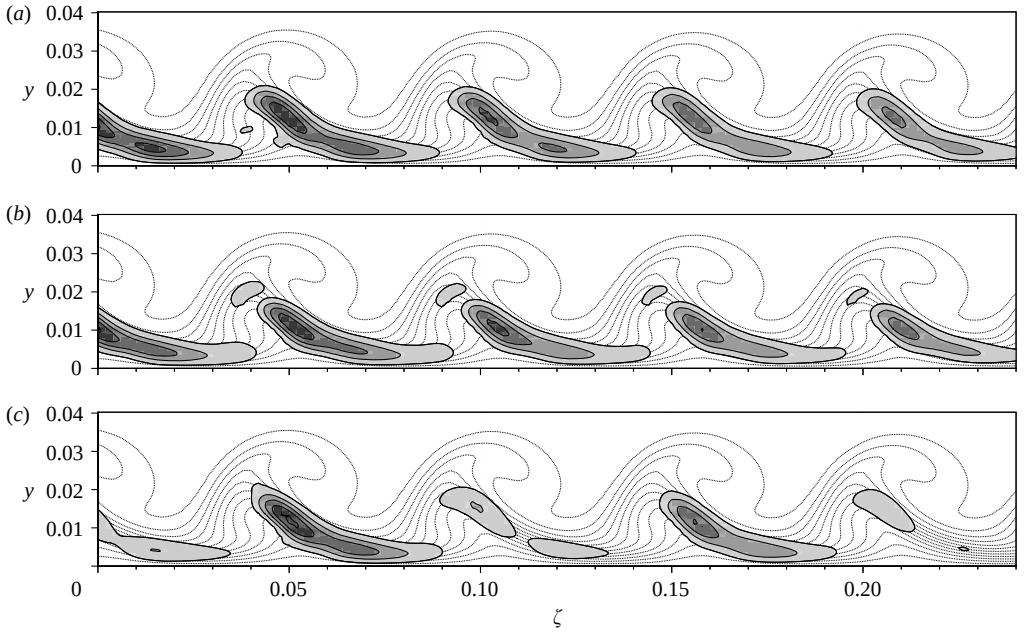

FIGURE 16. Isocontours of normalized $\tilde{u}_{s,h}$-amplitude in a cross-section in the vortex-oriented system for $\beta = 16$ at $\xi = 5.5$ for case CFV-med/TS-low: (*a*) subharmonic part, (*b*) fundamental part, (*c*) superposition of both. Isolines from 0.15 to 0.95 with a 0.2 spacing are shown and the deformed mean flow is indicated by the dotted lines.

growing of their amplitude maximum; both can be extracted by a t-modal flow-field decomposition. The amplitude distribution is not harmonic in the spanwise direction and can only be represented by a number of spectral modes, each with the same amplification rate. As examples, the secondary instabilities in classical crossflow induced transition in three-dimensional boundary layers or the secondary instabilities of Görtler vortices or streamwise streaks in two-dimensional boundary layers can be quoted here. In this sense, the disturbances developing in cases CFV-low/TS-low and CFV-med/TS-low are low-frequency secondary modes, and not 'locally amplified TS waves'.

5.3. *Laminar breakdown with small-amplitude CF vortices involved*

The saturated basic state in case CFV-low turned out to be not susceptible to high-frequency secondary instabilities. Therefore, to see breakdown in this case, the TS amplitude has been increased to 0.2 %, case CFV-low/TS-med (figure 17*a*). The t-modal amplitude development (figure 17*b*) shows the growth of all modes with TS frequency to a value of 25 % downstream of $x = 4.0$, and the generation and growth of higher-frequency harmonics to large values. In physical space, the strong wave pair identified in case CFV-low/TS-low leads to secondary vortices that lie obliquely to the primary CF vortex axis. They arise from the crests of the respective waves (figure 18). The vortices from each left-running wave are stronger first (see figure 18*a*). Eventually the vortices from each right-running wave are also visible, and a structure reminiscent of a Λ-vortex appears (figure 18*d*). Indeed, the right 'leg' has clockwise rotation when looking downstream, and the left one counter-rotates. Note however that, compared to a real two-dimensional base-flow situation, co-rotating primary vortices are present, one lying at about $\zeta = 0.04$ in figure 18; the chosen isocontour level is just too small

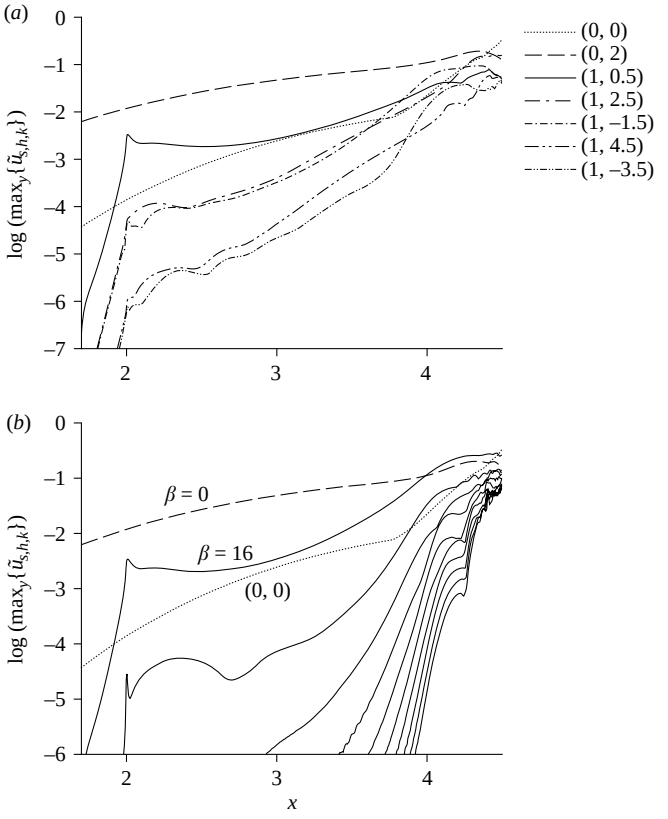

FIGURE 17. Downstream (a) (t-z)-modal and (b) t-modal ($\beta = 16 - 160$, $\Delta\beta = 16$) amplitude development in case CFV-low/TS-med.

to see. This vortex has a clockwise rotational motion, lying in between the secondary legs, and causes a flow-structure asymmetry by pulling the left leg upwards and the right leg down. The overlapping of the legs near their downstream tips is coincidental, and final breakdown is not connected with any formation of ring-like vortices ejected from connected tips, as is observed in the case of a Λ-vortex. Rather, tertiary vortices twine around the left leg, see figure 18c, $\xi = 5.6$, $\zeta = 0.01$ prior to final breakdown.

5.4. *Laminar breakdown with saturated CF vortices involved*

In case CFV-med, we have considered the naturally most amplified crossflow vortex mode as a primary disturbance, and it has been forced on a level not to saturate upstream of the APG region. With the small TS wave superposed, indications of a secondary instability have been found. Moreover, owing to the amplitude level of the vortex modes and the strong steady deformation of the flow, it may be supposed that the basic state is also susceptible to high-frequency secondary instabilities, which typically are much more strongly amplified than the TS amplification found in case CFV-med/TS-low. For the investigation of the transition mechanisms in this scenario, we have chosen a procedure already used in our former simulations. In addition to the saturated primary disturbances, we periodically force pulses of low-amplitude disturbances at various downstream positions to provide a background disturbance level for secondary instability. The periodic pulses, consisting of harmonic waves with discrete frequencies from $\beta = 10$ up to $\beta = 300$, $\Delta\beta = 10$ for $\gamma = \pm 22.5$,

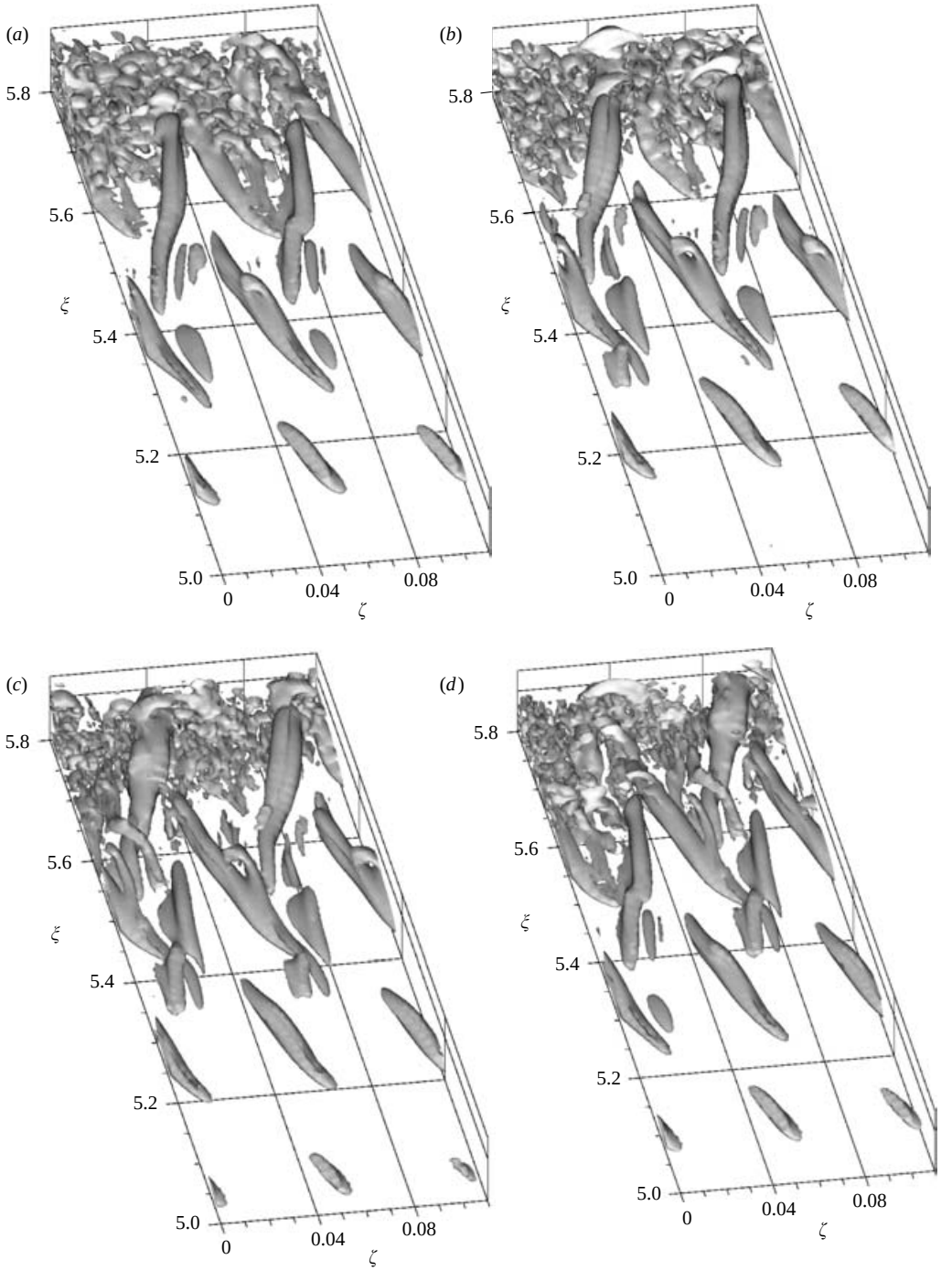

FIGURE 18. Visualization of vortical structures in the instantaneous flow fields for case CFV-low/TS-med, low-amplitude crossflow vortex mode plus TS wave, by λ_2-isosurfaces, $\lambda_2 = -50.0$. From (*a*) to (*d*): $t/T = 0$, 0.25, 0.5, 0.75; T – fundamental TS period ($\beta = 16$). Note the compression of the ξ-axis. For λ_2 see Jeong & Hussain (1995).

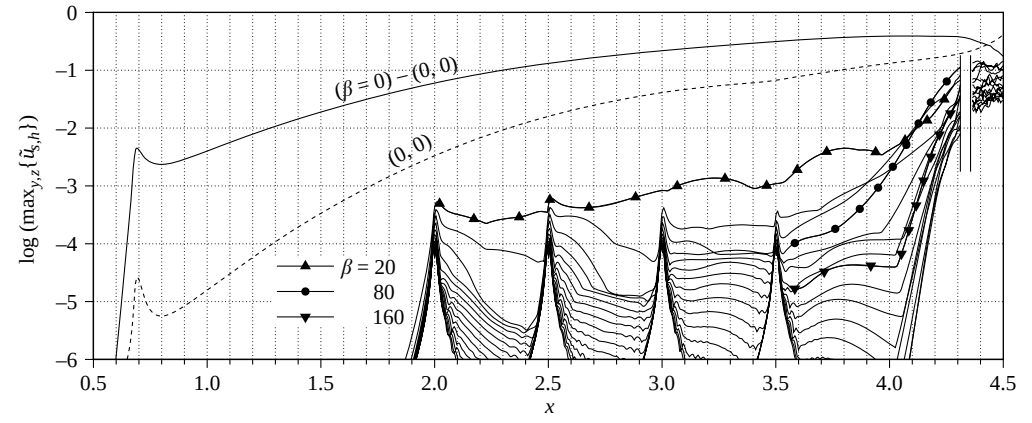

FIGURE 19. Downstream t-modal amplitude development for case CFV-med/pulses: crossflow vortex mode plus periodic background pulses. Frequencies from $\beta = 0$ to $\beta = 320$, $\Delta\beta = 20$ are shown. The curves to the left of the two vertical lines are found from second time-derivative analysis.

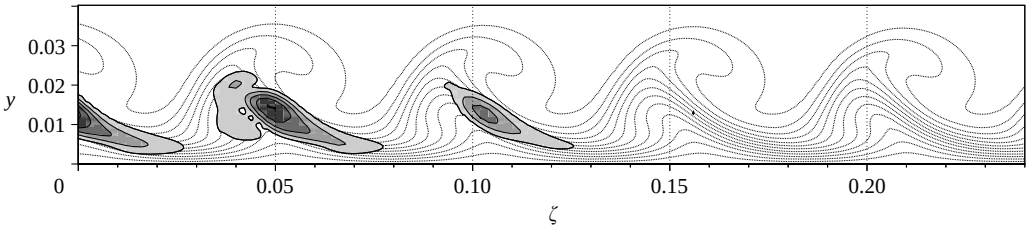

FIGURE 20. Isocontours of normalized $\tilde{u}_{s,h}$-amplitude in a cross-section in the vortex-oriented system for $\beta = 80$ at $\xi = 5.5$ for case CFV-med/pulses. Isolines from 0.15 to 0.95 with a 0.2 spacing are shown and the deformed mean flow is indicated by the dotted lines.

± 45.0 and ± 90.0 with $A_{(h,k)} = 5.0 \times 10^{-5}$ for each component, have been excited in case CFV-med/pulses at $x = 2.0$, 2.5, 3.0 and 3.5 to provide the full disturbance spectrum throughout the whole APG region. The disturbances are given for various spanwise wavenumbers in order to capture the range of TS instability as well as other instabilites.

The i-modal amplitude development (figure 19) shows that most of the background disturbances are damped upstream of $x = 3.5$. Only the low-frequency components ($\beta = 10,\ 20$) are weakly amplified, resulting in an amplitude growth of about one order of magnitude up to $x = 4.0$. A strong amplification can be first identified downstream of $x = 3.5$. Here the component $\beta = 80$ attains the largest amplitude in this region. The amplitude distribution, figure 20, clearly corresponds to the primary deformed basic state. Note that reducing ζ for constant ξ means increasing x, and the growth in the x-direction can be seen from right to left in this figure. As in case CFV-med/TS-low, the computational spanwise raster allows to analyse the fundamental ($\delta = 0$), subharmonic ($\delta = 0.5$) and detuned secondary instability modes ($\delta = 0.25,\ 0.75$). For any of the individual components, and their superposition, a very similar amplitude distribution can be found. Furthermore, figure 21 reveals that the growth of the respective modes is virtually identical.

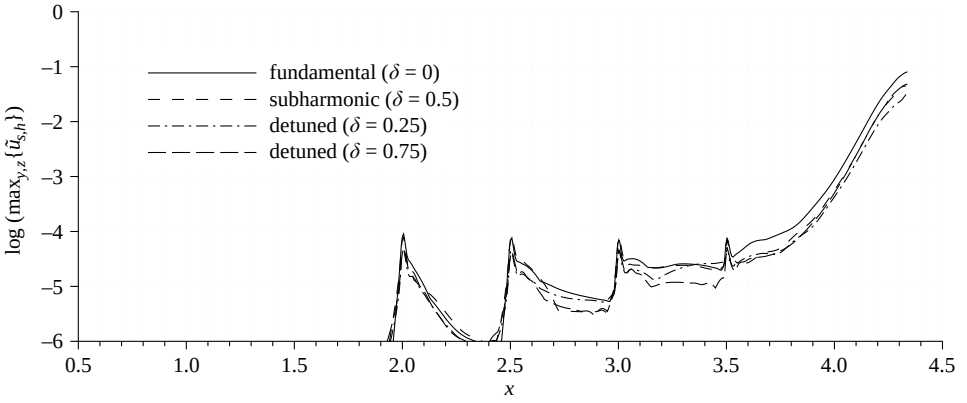

FIGURE 21. Downstream t-modal amplitude development for case CFV-med/pulses: crossflow vortex mode plus periodic background pulses. Comparison of the fundamental, subharmonic and detuned secondary instability modes for $\beta = 80.0$.

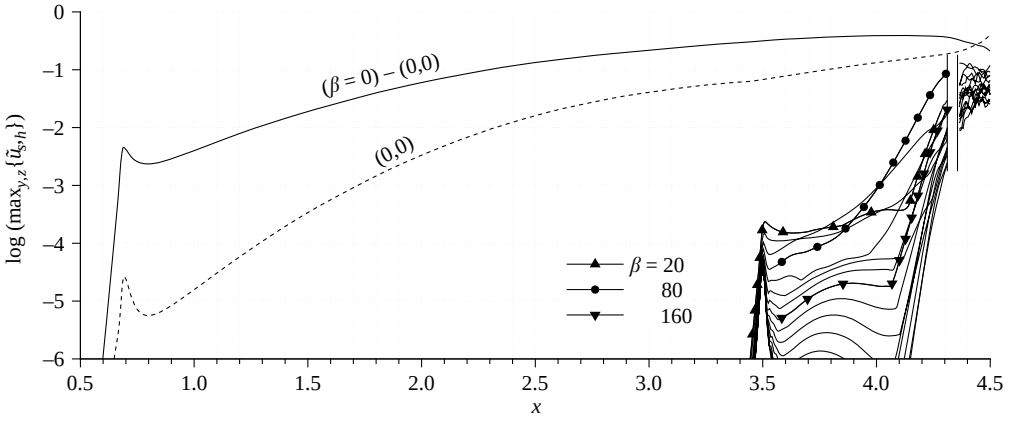

FIGURE 22. Downstream t-modal amplitude development for case CFV-med/pulsed: crossflow vortex mode plus periodic background pulses. Frequencies from $\beta = 0$ to $\beta = 320$, $\Delta\beta = 20$ are shown.

Therefore this simulation has been rerun with an excitation of the background pulses only at $x = 3.5$, and only for the fundamental spanwise wavenumber $\gamma = 90.0$ (case CFV-med/pulsed). The released computational resources could be spent for an improved spatial resolution of the late stages of the transition process.

In figure 22, the t-modal amplitude development is shown for the repeated simulation. After a short transient region, some disturbances undergo strong amplification, especially the component $\beta = 80$ which attains the largest amplitude downstream of $x = 4.0$. The low-amplitude mode with $\beta = 20$ is initially amplified rather weakly, as well as the high-amplitude modes ($\beta \approx 160$).

The cross-sections in figure 23 display the amplitude distributions of the respective secondary modes at two downstream positions. The first is at $\xi = 5.0$ corresponding to $x = 3.86$, and the second at $\xi = 5.5$, $x = 4.24$. The low-frequency mode with $\beta = 20$ first shows the typical shape for a mode of type III, a weakly amplified 'z' mode connected to the maximum of the spanwise gradient $\langle \partial \tilde{u}_s / \partial z \rangle$. Later on, this mode clearly is nonlinearly generated by high-frequency components resulting in the corresponding

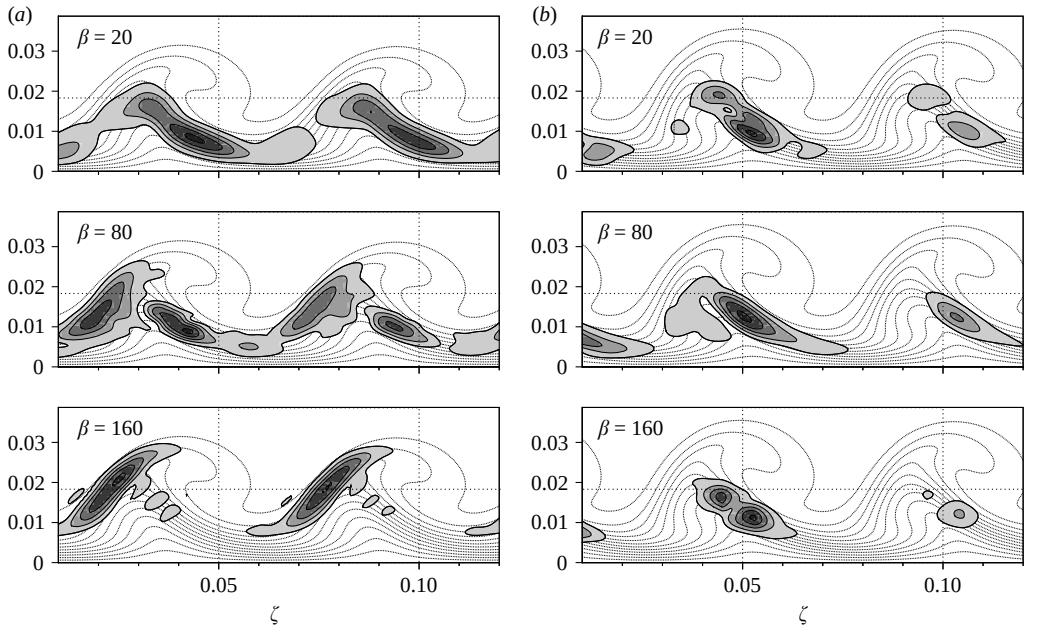

FIGURE 23. Isocontours of normalized $\tilde{u}_{s,h}$-amplitude for $\beta = 20$, $\beta = 80$ and $\beta = 160$ for case CFV-med/pulsed in a cross-section (ζ, y) at (*a*) $\xi = 5.0$ and (*b*) $\xi = 5.5$. Isolines from 0.15 to 0.95 with a 0.2 spacing are shown and the deformed mean flow is indicated by the dotted lines. To scale.

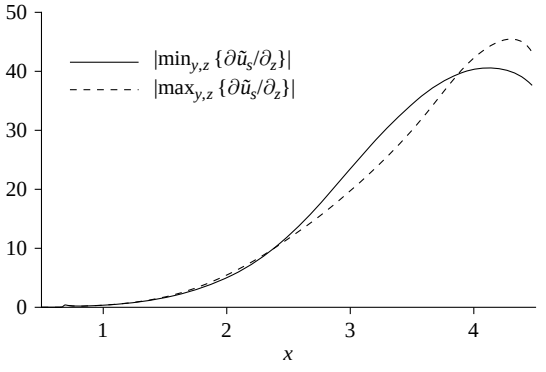

FIGURE 24. Downstream development of the minimum and maximum value of the spanwise gradient in the deformed mean flow in case CFV-med.

amplitude distribution. For the high-frequency component with $\beta = 160$, first rather weak amplification and the shape of a type I 'z' mode, connected to the minimum of $\langle \partial \tilde{u}_s / \partial z \rangle$, can be identified before further downstream it behaves and looks like the low-frequency mode.

The dominating mode with $\beta = 80$ is a superposition of two modes upstream of $x \approx 3.8$ until a clear type-III mode wins out and shows the strongest amplification of all the components. The shape coincides with the shape shown in figure 20 confirming that all important features are captured in the fundamental simulation. In the region of maximal amplification, the spatial amplification rate is nearly twice the maximal

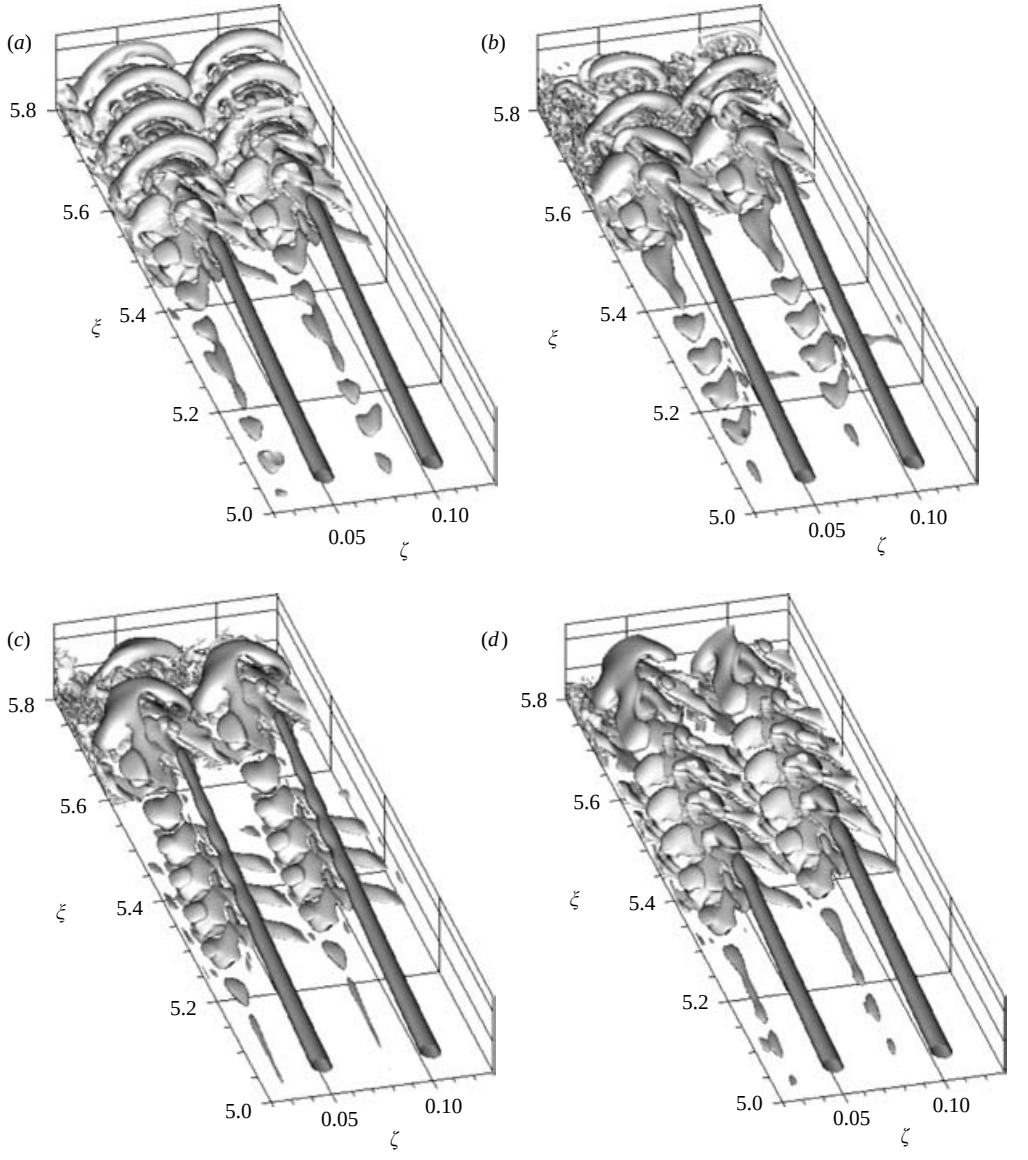

FIGURE 25. Visualization of vortical structures in the instantaneous flow fields for case CFV-med/pulsed, crossflow vortex mode plus periodic background pulses, by λ_2-isosurfaces, $\lambda_2 = -5.0$. From (*a*) to (*d*): $t/T = 0.0,\ 0.25,\ 0.5,\ 0.75$; T – period for $\beta = 10$. Approximately two spanwise wavelength are shown; note the compression of the ξ-axis.

amplification rate (of a type-I mode) or about six times the rate of the similar type-III mode as found in the corresponding scenario in the FPG region (cf. case 3B in Wassermann & Kloker 2002) Compared to the amplification of the low-frequency secondary mode in case CFV-med/TS-low it is more than four times larger. The competition of the two modes can be explained based on the development of the maximum and minimum value of the spanwise gradient (figure 24). Up to $x = 3.8$, the minimum value of the z-gradient is larger than the maximum value resulting in a dominance of the type-I mode. Further downstream, the ratio becomes reversed and

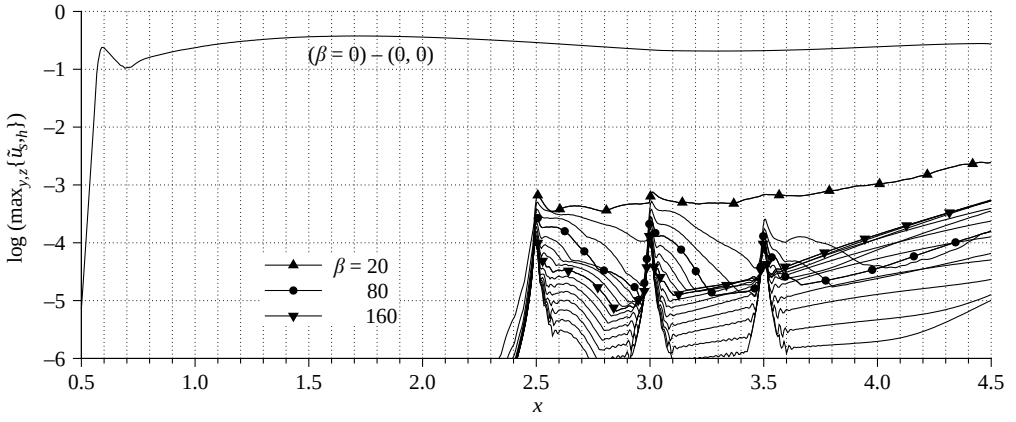

FIGURE 26. Downstream t-modal amplitude development for case UFD-high/pulses: crossflow vortex mode packet plus UFD plus periodic background pulses. Frequencies from $\beta = 0$ to $\beta = 320$, $\Delta\beta = 20$ are shown. The curves for $\beta > 0$ are obtained from second time-derivative analysis.

the type-III mode becomes dominant. Recall that the underlying mean flow possesses a growing positive crossflow near the wall that significantly influences the resulting streamwise velocity distribution of the primary state.

The competition process can also be identified looking on the corresponding structures in physical space visualized in figure 25. At $t/T = 0$ and $t/T = 0.25$ a cascade of structures can be seen, situated in the region of minimal spanwise gradient, clearly to the left of the steady vortices. Later on ($t/T = 0.5$), a cascade of three vortices underneath the primary vortices becomes visible. These vortices are situated in the region of maximal spanwise gradient, and they correspond to the type-III mode. Compared to the FPG scenario its frequency is five times the value of the primarily most amplified wave (FPG region: equal). We note that the seemingly staggered secondary vortex pattern is caused by rotation of the computed data, i.e. constant x is represented by a line that is tilted with respect to constant ξ, with the right-hand end lying at larger ξ than the left-hand end.

A dominant feature of the later stages is the appearance of an array of arc-type vortices riding on top of the steady CF vortices ($t/T = 0$). They are not a consequence of other modes and might be caused by a final type-II ($'y'$) instability. In plots of amplitude distributions, however, no distinct type-II mode could be identified.

5.5. *Influence of UFD vortices on the APG region*

In case UFD-high, a scenario resulting from the successful transition delay by means of an UFD is under investigation. According to case CFV-med/pulses the periodically pulsed low-amplitude background disturbances have been superimposed at $x = 2.5$, 3.0 and 3.5 for $\gamma = \pm 22.5$, ± 45.0 and ± 90.0 in case UFD-high/pulses, see figure 26. It turns out that this scenario is virtually stable with respect to TS instabilities, and also with respect to crossflow-vortex induced secondary instabilities. For the forced high-frequency background disturbances, only-weak amplification can be observed within the downstream part of the integration domain. Compared to case CFV-med/pulses this amplification is indeed rather low. How far downstream this effect persists is presently unclear and remains to be investigated. In the undisturbed APG region,

CF vortex modes are eventually amplified that have a different sense of rotation compared to the oncoming vortices because the basic crossflow has turned.

6. Conclusions

Spatial direct numerical simulations have been used to investigate likely breakdown scenarios in the adverse-pressure-gradient region of a three-dimensional boundary-layer flow with preceding favourable pressure gradient. The results obtained are:

(i) The reversed basic crossflow close to the wall leads to a redistribution of spanwise shear in the mean flow distorted by the steady crossflow vortices coming from upstream. The maximal positive z-gradient of u_s is now larger than the maximal negative gradient.

(ii) In the presence of a low-amplitude crossflow vortex, a TS wave, unstable or not, generates a three-dimensional wave pair of equal frequency that travels along the vortex. Once initiated, this pair grows autonomously by secondary instability. Thus the TS wave, unaltered by the vortex, is a catalyst for inducing a quasi-optimal secondary-instability mode, but is not necessary to sustain its growth as is the case in K-breakdown.

(iii) On travelling downstream, this wave pair evolves into obliquely oriented contra-rotating secondary vortices, one to the left-hand and one to the right-hand side of each primary vortex. By the primary-vortex motion, the downstream tip of the right-hand one is pressed down while the left-hand one is lifted up. Despite both structures seemingly forming a kind of Λ-shape, their tips are not connected and final breakdown is not induced as in the two-dimensional baseflow situation with a Λ-vortex. Rather, tertiary vortices twining around the secondary structures are harbingers of final breakdown.

(iv) In the presence of a medium-amplitude vortex, the TS wave generates a spanwise spectrum of equally important wave pairs with TS frequency that form a localized secondary instability mode. The TS wave itself is somewhat hindered in growth.

(v) The additional excitation of background pulses within a broad frequency band reveals that a secondary mode with five times the TS frequency is amplified most. This mode is of type III, connected with the region of maximal positive spanwise gradient of u_s, and its amplification is twice the value of the most amplified type-I mode in the favourable-pressure-gradient region; its frequency is half the corresponding value.

(vi) Final breakdown is accompanied by an array of vortex arcs on top of each primary vortex, which may indicate a final type-II-mode instability.

(vii) The amplification of detuned modes, i.e. modes with spanwise wavelengths larger than the spanwise vortex spacing, could be observed. These modes possess a (timewise) phase shift from vortex to vortex. As found also by other authors, their growth is similar. In very special situations, the superposition of, for example, a subharmonic and a fundamental mode of equal amplitude can lead to a local cancellation of disturbance activity at every second primary vortex. However we strongly believe that under most conditions, secondary instability appears as a localized event triggered whenever the local shear is large enough. A superposition of a wealth of detuned modes will just lead to an imperfectly synchronized activity at each successive vortex in the spanwise direction.

(viii) As for the often discussed 'active control of TS modes' in the APG region, it is evident that any growth of steady CF vortex modes should be hindered before. Then, methods aimed only at reducing two-dimensional TS waves running in the local

streamline direction are likely to fail. Three-dimensional modes must be targeted within a crosswise spectrum of modes, their frequencies ranging eventually up to five times the most amplified TS-frequencies.

(ix) The passive upstream flow deformation (UFD) technique, with forcing of subcritical-wavelength CF vortices in the early FPG region, turns out to keep its effectiveness in the considered APG region. However, the DNS performed can only show this effect in principle, within a relatively short streamwise region. In the real situation on an airfoil, it depends on how far downstream the UFD vortices are persistent and beneficial. The reversed crossflow and the varying dispersion properties, including the effect of surface curvature, give rise to amplification of different CF vortex modes, that may have a reversed sense of rotation and interact with the modes from upstream. It is conceivable that beneficial modes could be excited and kept on the necessary amplitude level by repeated adapted excitation. This can work if the spanwise wavelength of the dangerous, naturally most amplified mode does not significantly decrease downstream. At this time, further experiments, in the laboratory or in flight, are essential.

REFERENCES

Andersson, P., Brandt, L., Bottaro, A. & Henningson, D. S. 2001 On the breakdown of boundary layer streaks. *J. Fluid Mech.* **428**, 29–60.

Bake, S., Meyer, D. G. W. & Rist, U. 2002 Turbulence mechanism in Klebanoff-transition. A quantitative comparison of experiment and direct numerical simulation. *J. Fluid Mech.* **459**, 217–243.

Bertolotti, F. P. 2000 On the connection between crossflow vortices and attachment-line instabilities. In H. F. Fasel & W. S. Saric (ed.) *Laminar-Turbulent Transition. Proc. IUTAM Symposium Sedona, USA (1999)*. Springer.

Chernoray, V. G., Bakchinov, A. A., Kozlov, V. V. & Löfdahl, L. 2001 Experimental study of the K-regime of breakdown in straight and swept wing boundary layers. *Phys. Fluids* **13**, 2129–2132.

Cossu, C. & Brandt, L. 2002 Stabilization of Tollmien–Schlichting waves by finite amplitude optimal streaks in the Blasius boundary layer. *Phys. Fluids* **14**, L57–L60.

Crouch, J. D. & Ng, L. L. 2000 Variable N-factor method for transition prediction in three-dimensional boundary layers. *AIAA J.* **38**, 211–216.

Jeong, J. & Hussain, F. 1995 On the identification of a vortex. *J. Fluid Mech.* **285**, 69–94.

Joslin, R. D. 1998 Aircraft Laminar Flow Control. *Annu. Rev. Fluid Mech.* **30**, 1–29.

Kachanov, Y. S. 1994 Physical mechanisms of laminar boundary-layer transition. *Annu. Rev. Fluid Mech.* **26**, 411–482.

Koch, W., Bertolotti, F. P., Stolte, A. & Hein, S. 2000 Nonlinear equilibrium solutions in a three-dimensional boundary layer and their secondary instability. *J. Fluid Mech.* **406**, 131–174.

Malik, M. R., Li, F., Choudhari, M. M. & Chang, C.-L. 1999 Secondary instability of crossflow vortices and swept-wing boundary-layer transition. *J. Fluid Mech.* **399**, 85–115.

Messing, R. & Kloker, M. 2003 DNS study of discrete suction in a 3-d boundary layer. In S. Wagner, M. Kloker & U. Rist, (ed.) *Recent Results in Laminar–Turbulent Transition.* Selected numerical and experimental contributions from the DFG priority programme 'Transition' in Germany, NNFM vol. 86, pp. 177–188. Springer.

Saric, W. S., Carrillo, R. B. & Reibert, M. S. 1998*a* Leading-edge roughness as a transition control mechanism. *AIAA Paper* 98-0781.

Saric, W. S., Reed, L. H., White, E. B. 2003 Stability and transition of three-dimensional boundary layers. *Annu. Rev. Fluid Mech.* **35**, 413–440.

Spalart, P. R. 1993 Numerical study of transition induced by suction devices. In R. M. C. So, C. G. Speziale & B. E. Launders (ed.) *Proc. Intl Conf. Near-wall Turbulent Flows*, pp. 849–858, Tempe, Arizona, USA.

Spalart, P. R., Crouch, J. D. & Ng, L. L. 1994 Numerical study of realistic perturbations in 3-d boundary layers. In *Proc. AGARD Conf. Application of Direct and Large Eddy Simulation to Transition and Turbulence, Chania, Crete, Greece*. AGARD-CP-551, 30.1–30.10.

Theofilis, V., Fedorov, A., Obrist, D. & Dallman, U. Ch. 2003 The extended Görtler–Hämmerlin model for linear instability of three-dimensional incompressible swept attachment-line boundary layer flow. *J. Fluid Mech.* **487**, 271–313.

Wassermann, P. & Kloker, M. 2002 Mechanisms and passive control of crossflow-vortex induced transition in a three-dimensional boundary layer. *J. Fluid Mech.* **456**, 49–84.

Wassermann, P. & Kloker, M. 2003 Transition mechanisms induced by travelling crossflow vortices in a three-dimensional boundary layer. *J. Fluid Mech.* **483**, 67–89.